

FINITE ELEMENT MODEL DEVELOPMENT AND VALIDATION FOR AIRCRAFT FUSELAGE STRUCTURES

Ralph D. Buehrle, Gary A. Fleming and Richard S. Pappa
NASA Langley Research Center

and

Ferdinand W. Grosveld
Lockheed Martin Engineering and Sciences

18th International Modal Analysis Conference
San Antonio, Texas
February 7-10, 2000

FINITE ELEMENT MODEL DEVELOPMENT AND VALIDATION FOR AIRCRAFT FUSELAGE STRUCTURES

Ralph D. Buehrle, Gary A. Fleming and Richard S. Pappa
NASA Langley Research Center

and

Ferdinand W. Grosveld
Lockheed Martin Engineering and Sciences

Abstract

The ability to extend the valid frequency range for finite element based structural dynamic predictions using detailed models of the structural components and attachment interfaces is examined for several stiffened aircraft fuselage structures. This extended dynamic prediction capability is needed for the integration of mid-frequency noise control technology. Beam, plate and solid element models of the stiffener components are evaluated. Attachment models between the stiffener and panel skin range from a line along the rivets of the physical structure to a constraint over the entire contact surface. The finite element models are validated using experimental modal analysis results. The increased frequency range results in a corresponding increase in the number of modes, modal density and spatial resolution requirements. In this study, conventional modal tests using accelerometers are complemented with Scanning Laser Doppler Velocimetry and Electro-Optic Holography measurements to further resolve the spatial response characteristics. Whenever possible, component and subassembly modal tests are used to validate the finite element models at lower levels of assembly. Normal mode predictions for different finite element representations of components and assemblies are compared with experimental results to assess the most accurate techniques for modeling aircraft fuselage type structures.

Nomenclature

| | |
|--------|------------------------------------|
| ATC | Aluminum Testbed Cylinder |
| EOH | Electro-Optic Holography |
| ERA | Eigensystem Realization Algorithm |
| DOF(s) | degree(s) of freedom |
| FE | finite element |
| FRF(s) | frequency response function(s) |
| Hz | Hertz |
| MIF(s) | mode indicator function(s) |
| psig | pounds per square inch gauge |
| SLDV | Scanning Laser Doppler Velocimetry |

Introduction

Improved mid-frequency structural vibration and acoustic response predictions are required for design optimization and noise control applications in the aerospace and transportation industries. Finite element (FE) and boundary element methods are generally used for low frequency predictions where discrete modal behaviors dominate. Statistical energy analysis [1] and energy finite element

analysis [2] are used in the high frequency region, characterized by high modal density. In the mid-frequency region, the assumption of high modal density used in the energy analysis formulations is no longer valid. Finite element analysis in the mid-frequency region becomes more difficult because the structural vibration wavelength decreases with increasing frequency requiring a finer element mesh to describe the dynamic response. Advances in computer technology provide the capability to solve FE analyses of increasing complexity. In this paper, the ability to extend the valid frequency range for FE based structural dynamic predictions using detailed models of the components and attachment interfaces is examined. Normal mode predictions for different finite element representations of components and assemblies are compared with experimental results to assess the most accurate techniques for modeling aircraft fuselage type structures.

Hardware Description

This paper focuses on two stiffened aircraft fuselage structures. The first structure is the Aluminum Testbed Cylinder (ATC). Figures 1 and 2 show the primary components of the ATC. The cylindrical section of the ATC is an all-aluminum structure that is 12 feet in length and 4 feet in diameter. The shell consists of a 0.040-inch thick skin that is stiffened by 11 ring frames and 24 equally spaced longitudinal stringers. Double lines of rivets and epoxy are used to attach the skin to the frames and stringers. The floor is constructed of aluminum honeycomb and is supported by cross members at each of the ring frames. Two-inch thick particleboard end plates provide stiff, terminating reflective surfaces for the enclosed acoustic cavity. The end plates contain several ½-inch diameter holes to allow the pressure on each side of the end plates to equalize during pressurized tests. The end domes are ¼-inch thick fiberglass composite structures allowing for pressurization of the interior to 7 psig to simulate flight conditions at altitudes up to 35000 feet.

The second structure is an aluminum fuselage panel shown in Figure 3. The panel is representative of current aircraft construction but was manufactured without curvature to simplify the experimental and analytical modeling. The 47-by 72-inch aluminum panel consists of a 0.050-inch skin with six equally spaced longitudinal stringers and four equally spaced frame stiffeners. Single lines of rivets attach the stringers and frames to the skin. As shown in Figure 3, a bay is defined as a section of the panel skin that is bounded by the stringers and frames. The bay responses are the focus of the fuselage panel correlation efforts.

Numerical Modeling

Geometric and finite element models of the fuselage structures were developed in MSC/PATRAN. The models were generated based on the physical dimensions and material properties of the structures as specified in the manufacturing drawings. Normal mode analysis of the FE models was performed using the Lanczos method in MSC/NASTRAN.

A detailed description of the baseline ATC finite element model is provided by Grosveld [3]. FE models of an isolated ring frame and longitudinal stringer were developed using bar, beam, plate, and solid elements. In addition, a hybrid model combining beam and plate elements was used to provide the required load path near the cutouts in the ring frame while attempting to minimize the number of degrees of freedom (DOFs). Normal mode predictions for the component models are compared with modal test data to assess the required level of modeling detail.

The ATC framework, consisting of the interconnected ring frames and longitudinal stringers, was modeled using linear plate elements. Coincident nodes at the frame to stringer intersections were equivalenced. This constrains all six DOFs between the frames and stringers at these nodes. One motivation for using the 2-dimensional plate element for the frames and stringers is for the attachment of the skin. As described previously, the skin of the cylinder is attached to the frames and stringers using a double line of rivets and epoxy. The additional dimension provided by the plate elements allows the skin to be constrained over the width of the stiffener. In this way, each bay (unsupported skin section bounded by the frames and stringers) has the correct dimensions. A model of the baseline ATC including the cylinder frame with the skin attached was developed using linear plate elements. The coincident nodes at the stiffener to skin attachment locations were equivalenced. Normal mode predictions for the frame and baseline cylinder will be compared with modal test data.

Finite element modeling of the fuselage panel [4] has focused on different stiffener to skin attachment models and their effects on the predicted bay motions. To characterize the panel dynamic response up to 1000 Hz, several methods of modeling the panel were examined. First, the required finite element mesh density of the panel skin was evaluated by performing a normal mode analysis of a single bay with clamped boundary conditions. The skin was modeled with linear plate elements. A mesh of 30 by 16 elements was found to provide a one-percent convergence on frequency and adequate spatial resolution to define the mode shapes through 1000 Hz. This resulted in 11682 linear plate elements for the overall panel skin.

After establishing the model for the panel skin, three methods of modeling the stiffeners were evaluated. The simplest method is to model the stiffeners with beam elements. The beam elements are one-dimensional elements that have the effective cross-sectional properties (area, inertia's, and torsional constant) of the stiffeners. Offsets from the skin to the stiffener neutral axis are also included. The beam elements are created along a line consistent with the rivet line that attaches the skin to the

stiffeners. The beam stiffener model of the panel contains approximately 60,000 DOFs.

A second method of modeling the stiffeners is to use two-dimensional linear plate elements. This requires a detailed model of the geometry of the stiffeners. The plate element model of the stiffeners can then be attached to the skin elements over the entire contact surface or along a line consistent with the rivet line on the physical structure. Normal mode analyses were performed for both the surface and rivet line constraint. The plate stiffener model with rivet line attachment contains approximately 141,000 DOFs.

A third hybrid model of the stiffeners was generated to minimize the DOFs and provide the required load path near sections with cutouts. The frame sections with cutouts were modeled with plate elements and the stringers with continuous cross-sections were modeled with beam elements. For this model, the stiffener to skin attachment was along the rivet line. The hybrid stiffener model of the fuselage panel contains approximately 71,000 DOFs.

Experimental Validation

Experimental modal analysis results were used to validate the normal mode predictions of the various finite element models. Modal tests of an isolated ring frame and longitudinal stringer were performed to verify the ATC component models. These tests were conducted with the structures suspended from bungee chord to simulate free-free conditions. Frequency response functions (FRFs) were acquired between the four reference accelerometers and impact force. Sufficient impact positions were used to capture the modal properties over the 0 to 200 Hz frequency range. The polyreference curvefitter in the Spectral Dynamics STAR software was used to determine the modal properties from the FRF data.

To facilitate model updating, modal tests are planned for seven different levels of assembly for the ATC. Three assembly level modal tests have been conducted on the ATC [5]. First, the cylinder framework, composed of the interconnected ring frames and stringers, was tested prior to application of the skin. The second test configuration added the end plates to the cylinder frame. The third configuration is the baseline cylinder shown in figure 4, which is composed of the cylinder framework from configuration 1 with the skin applied. In each test configuration, the structure was supported by bungee chord to simulate free-free boundary conditions. The assembly level tests were conducted with multi-point random excitation and 207 accelerometer response measurements. The excitation and response measurement positions were selected based on pre-test predictions of the first 100 modes. FRFs were acquired over the 0 to 1000 Hz bandwidth. Because of the large number of modes excited in each test and the relatively low damping levels, Fourier transform block sizes as high as 64K were used. Mode indicator functions (MIFs) [6] were calculated from the FRFs to provide an estimate of the natural vibration frequencies of the structure. The Eigensystem Realization Algorithm (ERA) [7] was used to identify the modal parameters (natural frequencies, damping factors, and mode shapes) for each test configuration. Future tests of the ATC will incorporate the end plates, the domes, and the floor

(configurations 4, 5, and 6). Configuration 7 will include pressurization of the fully assembled ATC to simulate flight conditions. The effects of pressurization on the measured modal properties will be examined. Local bay modes of the structure will be the most affected by the pressurization. This will require higher spatial resolution, non-contacting measurement techniques for model validation.

The capabilities of two non-contacting measurement techniques were demonstrated on the 42- by 72-inch fuselage panel. For this study, validation of the predicted bay motions up to 1000 Hz was of primary interest. Scanning Laser Doppler Velocimetry (SLDV) and Electro-Optic Holography (EOH) measurement techniques were used to provide the required validation measurements.

Scanning Laser Doppler Velocimetry (SLDV) data was acquired on the fuselage panel by the United States Naval Research Laboratory [8]. Soft spring support was used to simulate free-free boundary conditions. An electromagnetic shaker mounted on the longitudinal stringer above the center bay excited the structure with a 30 to 2000 Hz chirp. Three-axis velocity measurements were acquired over a grid of 42 x 64 measurement points. This resulted in 2688 measurement points over the 47- by 72-inch panel. At each point, 32 time series ensembles of 16384-points were collected at a sample rate of 12.5 kHz. The laser was then moved to the next measurement point and the process of exciting the panel and measuring the time series ensembles was repeated. From the time series ensembles, the FRFs were calculated between the velocity and drive point force with a 0.763 Hz resolution. At each frequency of interest, the modal response of the panel was determined from the real part of the FRFs.

The Electro-Optic Holography (EOH) technique was used to measure the vibration modes of the center bay (Figure 3) of the fuselage panel [4]. EOH provides image-based, non-contacting quantitative measurements of the mean displacement amplitude of a vibrating structure. Current analysis methods are restricted to single frequency excitation. The panel was supported with bungee chords to simulate a free-free boundary condition. A piezoelectric actuator mounted on a longitudinal stringer just above the center bay provided sine excitation. The out-of-plane displacements of the center bay were observed on the computer screen and the input frequency was adjusted to maximize the displacements, indicating resonance for a given deformation pattern. Quantitative EOH measurements were obtained at 10 different resonant frequencies between 293.0 Hz and 831.7 Hz.

Discussion of Results

The predicted natural frequencies for the bar, beam, plate and solid element models of the ATC longitudinal stringer are compared with the measured frequencies in Table 1. For the beam, plate, and solid element models the predictions are in excellent agreement with the experimental results. The effects of the shear center offset are not included in the bar model and this leads to inaccurate results for the higher frequency y-axis bending modes. From the results of the plate and solid element models, it was observed that the higher frequency y-axis bending modes

begin to couple with torsional type motions. For this member with constant cross-sectional properties, the beam element model is sufficient to characterize the dynamics.

For the ATC ring frame, the numerical and experimental natural frequencies are listed in Table 2. One frequency is listed for each set of repeated roots, due to the ring frame symmetry. The number of bending waves (n) define the out-of-plane mode shapes. The number of circumferential waves (i) define the in-plane shell mode shapes. Differences of more than 30% occur for the beam element model of the ring frame. This is attributed to the effects of the ring frame cutouts (see Figure 2) where the stringers are attached. The beam elements in the cutout sections have the equivalent properties for the reduced section. However, this does not adequately model the complex load transmission path around the cutouts. The plate model results consistently underpredict the frequencies. The solid model is in good agreement with the experimental results, but is too large for use at higher levels of assembly. A hybrid model combining beam and plate elements was developed to characterize the load path around the cutouts while minimizing the DOFs. The hybrid model results are within 7% of the experimental results.

A representative frequency response function from the modal test on the ATC baseline cylinder is shown in figure 5. The mode indicator function for the baseline cylinder is shown in figure 6. The dips in the MIF (particularly those that extend to approximately zero) indicate the natural frequencies. From figures 5 and 6, it is easy to see the increasing modal density associated with the occurrence of the first bay mode at approximately 370 Hz. The high modal density is attributed to the 240 bays with the same nominal dimensions. This demonstrates the difficulties associated with FE model validation on a discrete mode basis in the mid-frequency region.

Comparisons for the numerical and experimental natural frequencies for the ATC framework and baseline cylinder are provided for the first fifteen modes in Tables 3 and 4. Mode shapes were identified for torsion, bending, shearing, and cylinder shell modes. The number of circumferential waves (i) and the number of axial half-waves (j) define the shell modes. Figure 7 shows the measured $i=3, j=2$ mode for the baseline cylinder. As shown in the Tables, the predicted frequencies are within 16% of the measured frequencies. The accurate prediction of the shell modes is of particular interest for the acoustics application. These modes tend to be in better agreement, within 9% with one exception. The FE models generally overpredict the natural frequencies. This indicates a FE model that is too stiff. The constraint of all DOFs at the intersection of the stiffeners and at the stiffener to skin attachments is believed to be partially responsible for this overprediction. Work is ongoing for the numerical prediction and experimental validation of higher frequency modes of the cylinder bay areas bounded by the frames and stringers.

Normal mode analysis of the panel finite element models results in 400 to 500 modes predicted in the 0 to 1000 Hz frequency range, depending on the stiffener model. The local bay modes of the panel are of primary importance for comparison with the EOH and SLDV data. The (l, m) mode

shape of a bay is defined by “l” half sine waves along the horizontal and “m” half sine waves along the vertical direction. Figure 8 shows the (3,1), (2,2) and (5,1) deformation shapes of the fuselage panel center bay measured using SLDV and EOH and predicted using the plate stiffener model with rivet line attachment. In the figure, the black and white represent peak amplitudes that are 180 degrees out-of-phase. The deformation shapes are consistent and the measured and predicted frequencies are within 8.3%. Interaction between the bays of the panel result in local modes appearing over a band of frequencies. This is shown in Figures 9 and 10, where the panel has the same (2,1) mode shape for a bay but different bay interactions. For the mode shape at 231.7 Hz, the motion of a bay is 180 degrees out-of-phase with adjacent bays in both the vertical and horizontal directions. The phase pattern for the 236.6 Hz mode has the bays in-phase along the vertical direction but 180 degrees out-of-phase along the horizontal direction. Similar mode shapes were observed in the SLDV data at 203.7 Hz and 238.8 Hz, respectively.

The validation of individual modes are complicated by the fact that similar bay deformation shapes appear over a range of frequencies due to the complex bay interactions. In an effort to provide a comparison between the predicted and experimental data, the natural frequencies corresponding to the most dominant response for a given bay deformation shape were selected. Figure 11 shows the predicted natural frequencies for the panel bay modes below 1000 Hz compared with the SLDV data. The plate stiffener model with surface attachment significantly overpredicts the natural frequencies above 500 Hz. This indicates the model is too stiff as compared to the actual panel. In contrast, the plate stiffener model with rivet line attachment is the most consistent with the SLDV data but tends to underpredict the natural frequencies.

Summary and Conclusions

The ATC modeling efforts yielded several significant findings. Beam element models are sufficient for characterizing the dynamic response of the continuous cross-section longitudinal stringers. However, at higher levels of assembly, plate element models of the stringers were required to incorporate a constraint over the width of the stiffener to skin attachment. This provides the correct dimensions for the bay areas bounded by the frames and stringers. Due to the complex load transmission path around the cutouts, higher order elements are required to characterize the dynamic response of the ring frame. ATC assembly level finite element models overpredict the natural frequencies. The constraint of all DOFs at the intersections of the stiffeners and at the stiffener to skin attachments is believed to be partially responsible for this overprediction. Validation of the ATC assembly level finite element models is continuing. Future tests will include the end plates, domes, and floor. Final phases of the program will examine the effects of pressurization on the ATC modal properties.

Several different finite element models of the fuselage panel were examined for the purpose of characterizing the dynamic response at frequencies up to 1000 Hz. This effort focused on different stiffener to skin attachment models and their effects on the predicted bay motions. Comparisons

between normal mode predictions and measured deformation shapes show that attachment models that constrain the skin over the entire contact surface with the stiffeners are too stiff. The best agreement with experimental results was obtained for the plate element model of the stiffeners with attachment to the skin along a line consistent with the rivet line of the physical structure. Predicted frequencies for the plate stiffener model with rivet line attachment were consistently lower than the measured frequencies. This indicates that further refinement of the model of the attachment interface is required. Modification of a large portion of the FE model may be required to incorporate additional details of the attachment interface.

Extending the frequency range of interest beyond traditional FE analysis results in a large number of modes, increased modal density, and increased spatial resolution requirements. This provides significant challenges for FE model validation on a discrete mode basis. SLDV and EOH techniques demonstrated their usefulness in providing increased spatial resolution for the high frequency model validation of a fuselage panel.

References

- [1] Burroughs, C. B., Fischer, R. W., and Kern, F. R., “An Introduction to Statistical Energy Analysis,” *Journal of Acoustical Society of America*, Volume 101, No. 4, April 1997, pp. 1779-1789.
- [2] Bouthier, O. M., and Bernhard, R. J., “Models of Space-Averaged Energetics of Plates,” *AIAA Journal*, Vol. 30, No. 3, March 1992, pp. 616-623.
- [3] Grosveld, F. W., “Structural Normal Mode Analysis of the Aluminum Testbed Cylinder (ATC),” *AIAA Paper 98-1949*, Proceedings of the 39th AIAA/ASME/ASCE Structures, Structural Dynamics, and Materials Conference, Long Beach, CA, April 1998.
- [4] Fleming, G. A., Buehrle, R. D., and Storaasli, O. L., “Modal Analysis of an Aircraft Fuselage Panel Using Experimental and Finite-Element Techniques,” Proceedings of the 3rd International Conference on Vibration Measurements by Laser Techniques, Ancona, Italy, June 1998.
- [5] Pappa, R. S., Pritchard, J. I., and Buehrle, R. D., “Vibro-Acoustics Modal Testing at NASA Langley Research Center,” *NASA/TM-1999-209319*, May 1999.
- [6] Williams, R., Crowley, J., and Vold, H., “The Multivariate Mode Indicator Function in Modal Analysis,” Proceedings of the 3rd International Modal Analysis Conference, Orlando, Florida, January 1985, pp. 66-70.
- [7] Pappa, R. S., “ERA Bibliography,” Website: http://sdb-www.larc.nasa.gov/SDB/Research/data/ERA_biblio.html, September 1998.
- [8] Vignola, J., and Houston, B. H., “A Three-Dimensional Velocity Measurement of a Periodically Ribbed Aircraft Panel Surface by Optical Vibrometry,” Proceedings of the 3rd International Conference on Vibration Measurements by Laser Techniques, Ancona, Italy, June 1998.

Table 1. Experimental and numerical natural frequencies for the longitudinal stringer

| Stringer mode shape | Measured frequency | Bar model | | Beam model | | Solid model | | Plate model | |
|---------------------------|--------------------|-----------|-------|------------|-------|-------------|-------|-------------|-------|
| | [Hz] | freq. | error | freq. | error | freq. | error | freq. | error |
| 1 st z bending | 8.8 | 9.085 | 3.2 | 9.02 | 2.5 | 9.10 | 3.4 | 9.15 | 4.0 |
| 1 st y bending | 9.3 | 9.773 | 5.1 | 9.57 | 2.9 | 9.70 | 4.3 | 9.72 | 4.5 |
| 2 nd z bending | 24.6 | 25.03 | 1.7 | 24.85 | 1.0 | 25.07 | 1.9 | 25.20 | 2.4 |
| 2 nd y bending | 26.2 | 26.90 | 2.7 | 25.74 | -1.8 | 26.12 | -0.3 | 25.89 | -1.2 |
| 3 rd z bending | 47.7 | 49.04 | 2.8 | 48.68 | 2.0 | 49.11 | 3.0 | 49.38 | 3.5 |
| 3 rd y bending | 48.4 | 52.63 | 8.7 | 48.62 | 0.4 | 49.50 | 2.3 | 48.62 | 0.4 |
| 4 th y bending | 76.2 | 86.77 | 13.9 | 76.44 | 0.3 | 78.35 | 2.8 | 75.96 | -0.3 |
| 4 th z bending | 78.5 | 81.01 | 3.2 | 80.42 | 2.4 | 81.10 | 3.3 | 81.58 | 3.9 |
| 5 th y bending | 108.5 | 129.19 | 19.1 | 107.5 | -0.9 | 111.53 | 2.8 | 106.60 | -1.8 |
| 5 th z bending | 117.2 | 120.91 | 3.2 | 120.0 | 2.4 | 120.98 | 3.2 | 121.79 | 3.9 |
| 6 th y bending | 144.8 | 179.12 | 23.7 | 141.0 | -2.6 | 148.53 | 2.6 | 139.83 | -3.4 |
| 6 th z bending | 163.4 | 168.72 | 3.2 | 167.5 | 2.5 | 168.64 | 3.2 | 169.96 | 4.0 |

Table 2. Experimental and numerical natural frequencies for the ring frame

| Ring frame mode shape | Measured frequency | Beam model | | Solid model | | Plate model | | Hybrid model | |
|-----------------------|--------------------|------------|-------|-------------|-------|-------------|-------|--------------|-------|
| | [Hz] | freq. | error | freq. | error | freq. | error | freq. | error |
| Out-of-Plane, n=2 | 9.84 | 14.01 | 42.4 | 9.63 | -2.1 | 8.0 | -18.7 | 10.50 | 6.71 |
| Out-of-Plane, n=3 | 31.47 | 45.26 | 43.8 | 30.90 | -1.8 | 26.1 | -17.1 | 33.22 | 5.56 |
| Out-of-Plane, n=4 | 63.49 | 91.02 | 43.4 | 62.43 | -1.7 | 53.2 | -16.2 | 66.44 | 4.65 |
| Out-of-Plane, n=5 | 104.81 | 147.55 | 40.8 | 102.63 | -2.1 | 87.3 | -16.7 | 108.44 | 3.46 |
| Out-of-Plane, n=6 | 153.73 | 211.20 | 37.4 | 150.02 | -2.4 | 127.0 | -17.4 | 157.46 | 2.43 |
| In-Plane, i=2 | 34.30 | 45.51 | 32.7 | 32.78 | -4.4 | 31.3 | -8.7 | 35.64 | 3.91 |
| In-Plane, i=3 | 97.95 | 129.27 | 32.0 | 93.67 | -4.4 | 88.7 | -9.4 | 101.44 | 3.56 |
| In-Plane, i=4 | 186.29 | 246.37 | 32.3 | 178.41 | -4.2 | 167.9 | -9.9 | 192.11 | 3.12 |

Table 3. First fifteen experimental and numerical natural frequencies for the ATC framework

| Analysis | Modal Test | Mode Description | Analysis /Test |
|----------------|----------------|---------------------|----------------|
| Frequency [Hz] | Frequency [Hz] | | Error [%] |
| 11.020 | 9.923 | 1st torsion mode | 11.06 |
| 18.724 | 16.292 | 1st x bending mode | 14.93 |
| 18.724 | 16.745 | 1st y bending mode | 11.82 |
| 25.296 | 21.950 | 1st x shearing mode | 15.24 |
| 25.296 | 22.546 | 1st y shearing mode | 12.20 |
| 25.581 | 22.803 | 2nd torsion mode | 12.18 |
| 29.694 | 29.363 | i=2, j=1 mode (1) | 1.13 |
| 29.694 | 29.418 | i=2, j=1 mode (2) | 0.96 |
| 36.145 | 31.491 | 2nd x bending mode | 14.78 |
| 36.145 | 31.746 | 2nd y bending mode | 13.86 |
| 35.564 | 34.213 | i=2, j=2 mode (1) | 3.95 |
| 35.564 | 34.427 | i=2, j=2 mode (2) | 3.30 |
| 44.354 | 38.542 | 3rd torsion mode | 15.08 |
| 46.164 | 42.655 | i=2, j=3 mode (1) | 8.23 |
| 46.165 | 42.969 | i=2, j=3 mode (2) | 7.44 |

Table 4. First fifteen experimental and numerical natural frequencies for the ATC baseline cylinder

| Analysis | Modal Test | Mode Description | Analysis /Test |
|----------------|----------------|------------------------|----------------|
| Frequency [Hz] | Frequency [Hz] | | Error [%] |
| 54.648 | 50.820 | i=2, j=0 Rayleigh (1) | 7.53 |
| 54.648 | 51.176 | i=2, j=0 Rayleigh (2) | 6.78 |
| 57.688 | 53.462 | i=2, j=0 Love mode (1) | 7.91 |
| 57.688 | 54.287 | i=2, j=0 Love mode (2) | 6.26 |
| 110.73 | 100.146 | i=2, j=1 mode (1) | 10.57 |
| 110.73 | 102.123 | i=2, j=1 mode (2) | 8.43 |
| 148.59 | 141.375 | i=3, j=1 mode (1) | 5.10 |
| 148.59 | 142.348 | i=3, j=1 mode (2) | 4.39 |
| 161.92 | 152.390 | i=3, j=2 mode (1) | 6.25 |
| 161.92 | 152.411 | i=3, j=2 mode (2) | 6.24 |
| 172.43 | 160.102 | i=3, j=3 mode (1) | 7.70 |
| 172.43 | 161.829 | i=3, j=3 mode (2) | 6.55 |
| 198.93 | 183.553 | i=3, j=4 mode (1) | 8.38 |
| 198.93 | | i=3, j=4 mode (2) | |
| 230.12 | 204.342 | i=2, j=2 mode (1) | 12.62 |

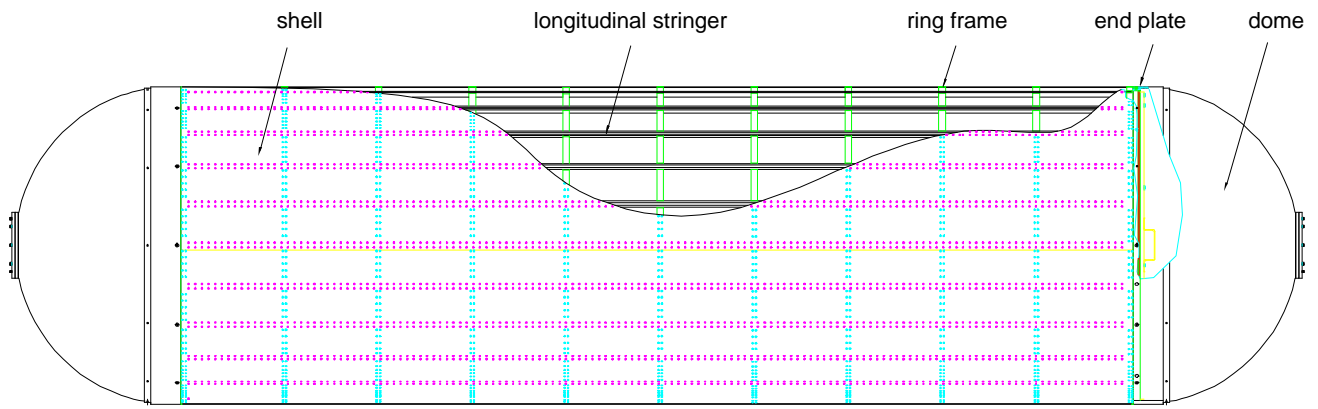


Figure 1. Aluminum Testbed Cylinder primary components.

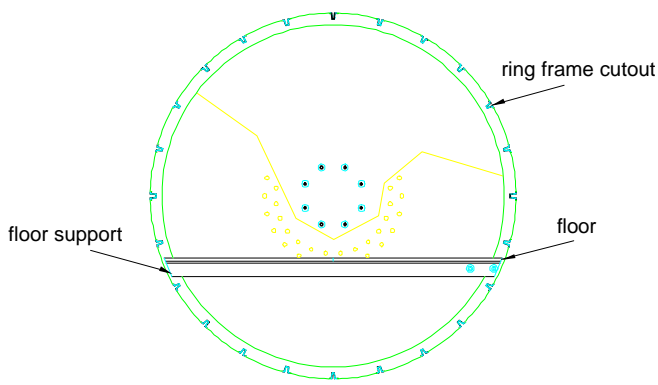


Figure 2. End view of Aluminum Testbed Cylinder showing ring frame, floor and floor support.



Figure 4. Modal test setup for baseline configuration of the Aluminum Testbed Cylinder.



Figure 3. Fuselage panel showing vertical frames, longitudinal stringers, center bay, and exciter location.

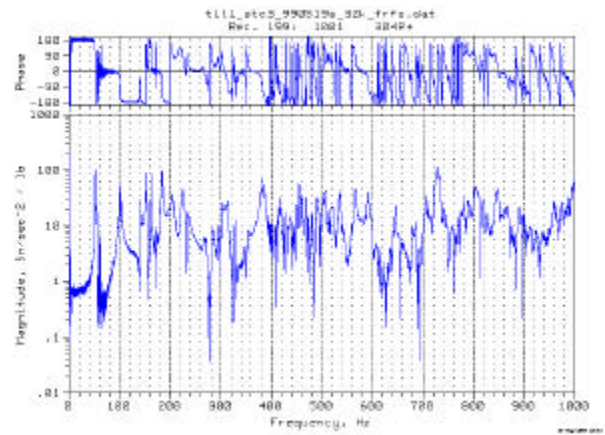


Figure 5. Typical frequency response function from modal test of baseline Aluminum Testbed Cylinder.

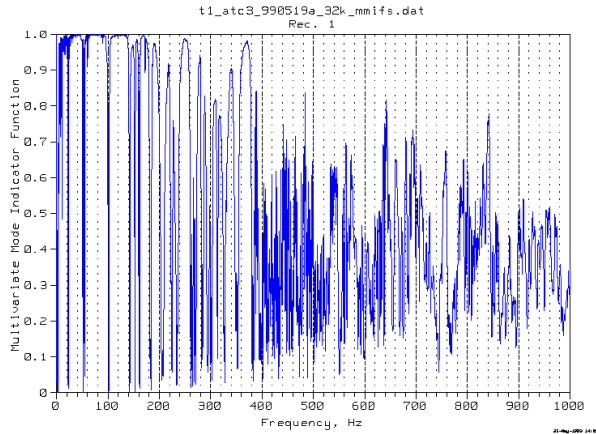


Figure 6. Mode indicator function for baseline configuration of Aluminum Testbed Cylinder.

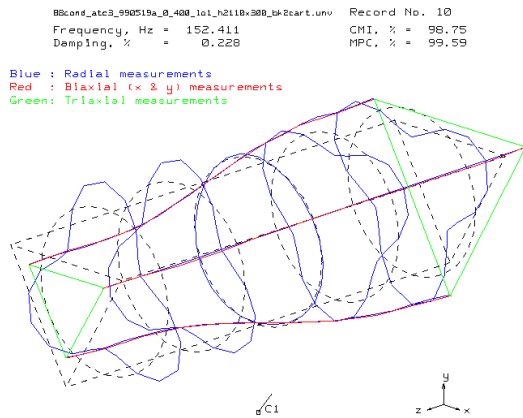


Figure 7. Measured circumferential-axial (3,2) cylinder mode for the baseline Aluminum Testbed Cylinder.

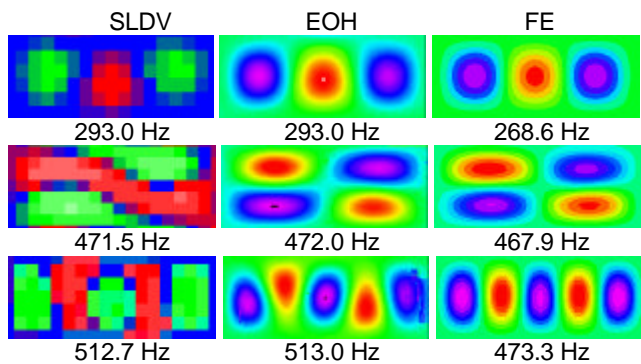


Figure 8. Measured and predicted (3,1), (2,2), and (5,1) deformation shapes for the fuselage panel center bay.

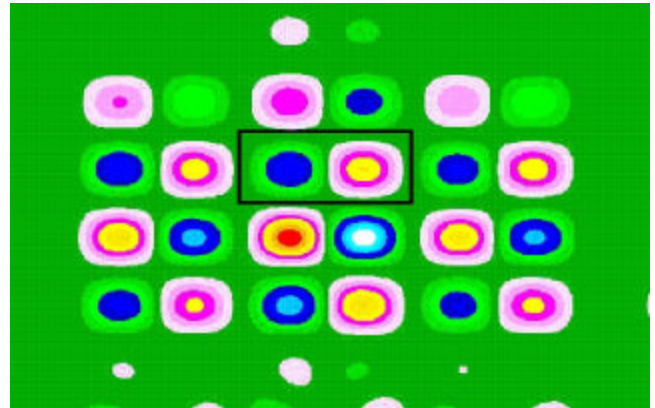


Figure 9. Predicted fuselage panel mode at 231.7 Hz showing (2,1) bay mode with out-of-phase deformation of adjacent bays in vertical and horizontal directions. Note the rectangular box that outlines the center bay.

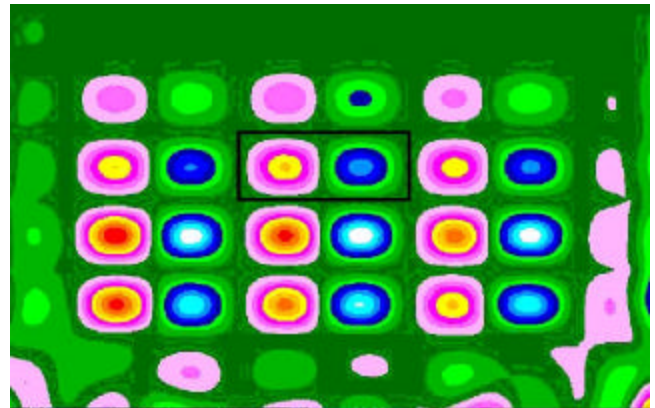


Figure 10. Predicted fuselage panel mode at 236.6 Hz showing (2,1) bay mode with in-phase deformation of adjacent bays in the vertical direction and out-of-phase deformation along horizontal direction. Note the rectangular box that outlines the center bay.

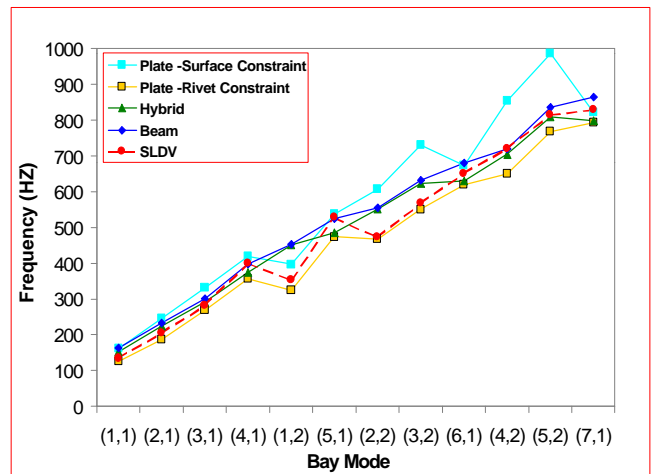


Figure 11. Comparison of predicted frequencies with measured (SLDV) frequencies.